ResearchGate

See discussions, stats, and author profiles for this publication at: https://www.researchgate.net/publication/311244781

The sensitivity of filtered Two Fluid Models to the underlying resolved simulation setup

Article *in* Powder Technology · April 2017

CITATIONS
0

READS
2

5 authors, including:

Jan Hendrik Cloete
Norwegian University of Science and Technol…

8 PUBLICATIONS **1** CITATION

SEE PROFILE

Schalk Cloete
SINTEF

52 PUBLICATIONS **261** CITATIONS

SEE PROFILE

Stefan Radl
Graz University of Technology

98 PUBLICATIONS **394** CITATIONS

SEE PROFILE

Some of the authors of this publication are also working on these related projects:

Project

Cleanroom Technology - Teaching View project

All content following this page was uploaded by Jan Hendrik Cloete on 01 December 2016.

The user has requested enhancement of the downloaded file. All in-text references underlined in blue are linked to publications on ResearchGate, letting you access and read them immediately.

The sensitivity of filtered Two Fluid Models to the underlying resolved simulation setup

Jan Hendrik Cloete[1], Schalk Cloete[2], Federico Municchi[3], Stefan Radl[3], Shahriar Amini[1,2]*

1) Department of Energy and Process Engineering, Norwegian University of Science and Technology (NTNU), NO-7491 Trondheim, Norway

2) Flow Technology Department, SINTEF Materials and Chemistry, NO-7465 Trondheim, Norway

3) Institute of Process and Particle Engineering, Graz University of Technology, Inffeldgasse 13/III, Graz, Austria

*Corresponding author. Email: shahriar.amini@sintef.no

Address: SINTEF Materials and Chemistry, S.P. Andersens vei 15 B, 7031 Trondheim, Norway, Phone: +47 46639721

Abstract

The filtered two fluid model (fTFM) is a promising approach for enabling large scale fluidized bed reactor simulations using multiphase flow modelling. A substantial amount of research has been conducted in this field to derive filtered closures for all applicable transport processes including drag, stresses, heat transfer, scalar transport and reactions. This work aims to investigate the effect of TFM closures used in the resolved simulations from which fTFM closures are derived in order to assess the degree of uncertainty stemming from this source. In addition, the filtering approach provides a good platform for building a detailed understanding of the effects of different TFM closures. Simulations showed that the drag model used in the resolved simulations had the most significant effect on the filtered quantities derived. Inclusion of a frictional pressure model also had a large influence in the dense regions of the domain. Selection of a more generic drag model and inclusion of a frictional pressure model is therefore recommended for future studies. Finally, results revealed that the effects of TFM closures on filtered quantities could be grouped into two categories: interphase transport (drag, heat transfer and reactions) and diffusive transport (stresses and scalar transport). This suggests a common methodology in terms of filtered model form for these two groups.

Keywords: Fluidised bed, Kinetic Theory of Granular Flow, Filtered Two-Fluid Model, Industrial scale simulations, Coarse-grid simulations

1 Introduction

The use of computational fluid dynamics (CFD) has become popular for studying fluidized bed reactors due to its ability to provide detailed information about the flow behaviour, which is difficult to obtain from experiments. One of the popular CFD approaches is the Two-Fluid model (TFM). In this approach,

the Kinetic Theory of Granular Flow (KTGF) [1-3] is often applied for fluidised beds. Within such a TFM-KTGF approach the solid phase is treated as a continuum, and the fluctuation of the particle velocities (i.e., the granular temperature) is predicted in order to close the granular stress tensor. Most important, KTGF relies on transport equations that assume that the granular flow field is well resolved, i.e., that the gas-particle mixture is homogeneous on a sub-grid scale.

However, the hydrodynamic behaviour of fluidized beds is characterized by the presence of transient multiphase structures such as bubbles in dense beds, and solid clusters in dilute risers. The behaviour of these structures determines many important aspects of fluidized bed operation, such as the bed expansion and the heterogeneous reaction rate. To accurately predict fluidized bed behaviour with the KTGF, one must therefore be able to resolve these complex multiphase structures. For large, industrial scale fluidized beds this remains unfeasible even with today's computational power, especially for finer particle sizes [4].

To overcome this obstacle, various researchers have proposed sub-grid scale corrections, such as the energy minimization multi-scale (EMMS) approach [5] or the filtered TFM (fTFM) [6, 7]. In these methods, the simulations are performed on a computationally affordable (i.e., coarse) grid. Constitutive equations are then solved that account for the effect that unresolved transient structures have on properties such as the drag, stresses, reaction rates, etc. In the fTFM, these constitutive equations are obtained by performing resolved simulations and then applying spatial averaging operations on differently sized filter regions. The size of these regions is related to the grid size used when running fTFM-based (i.e., “coarse grid”) simulations. Primarily three groups have been working on the development of this modelling technique using slightly different approaches; INPT [7, 8], Princeton [6, 9-13] and Linz [14, 15].

In this study, the Princeton approach will be followed and therefore requires more detailed discussion. Initial work focussed on flow situations in periodic domains [6, 9], and the sub-grid corrections for the drag, as well as the solids stresses, were correlated with the filtered particle phase volume fraction. The latter is called a “marker” in what follows. Later, these models were improved to include the effect that reactor walls have on the above constitutive equations [10], thereby making these models applicable to practical fluidized bed simulations. Later work produced correlations for sub-grid corrections of the heat/mass transfer rate [13], the scalar diffusivity [13], as well as first-order, heterogeneous reactions [11]. However, these studies were limited to 2D simulations and periodic simulations without walls. Finally, improvements were made to the hydrodynamic closures by adding the filtered slip velocity as a marker for the drag, as well as the filtered shear rate for the sub-grid solid stresses [12].

Despite these promising developments, numerous research questions remain unanswered in this field. One such research question is related to the effect that the choice of TFM closures used in the resolved simulations has on the correlations that are developed. This is a critical topic, since the fTFM constitutive models can only be as accurate as the TFM simulations from which they were derived. The TFM approach involves several important closure laws, each with a range of alternative formulations published over the past three decades. In addition, system-dependent coefficients such as the particle-particle restitution can potentially influence TFM model results. It is therefore important to understand the effect of TFM closures on filtered quantities in order to assess the uncertainty involved when applying the fTFM approach.

Another benefit of comparing filtered quantities derived from different TFM setups is that it can create a better understanding of how different closure choices influence simulation results. Traditionally, the sensitivity of simulation results to different closures is tested by performing expensive reactor simulations. Then, a variety of integral performance criteria, such as the average bed expansion, solids mass flux or conversion are compared for the different simulations [16]. Unfortunately, many interacting properties will influence these traditionally-used integral reactor performance criteria, thereby obscuring the detailed influences of changing the closures. Also, these integral criteria may be obscured by the typically too coarse computational grid resolution in reactor-scale simulations. Clearly, comparing different filtered quantities, differentiated by one or more markers and obtained in small, but well-resolved simulations, may improve the meaning of such studies. We argue that such an approach will lead to a better understanding of how and in which areas of operation simulation results are affected.

For this reason, this study will investigate the effect of several TFM closures and properties on filtered quantities, including corrections to the drag, solid stresses, heat transfer rate, reaction rate, and the dispersion of a scalar. The TFM options considered are the choice of drag law, inclusion of a frictional pressure model, the value of the particle-particle restitution coefficient used, and the choice of closure for the radial distribution function in the KTGF. It should be noted that other factors, not related to the choice of resolved TFM closures, such as the particle size and the simulation setup (period box or full reactor) may also introduce uncertainty in the filtered models [17], but were not considered in this study. For simplicity, the only marker considered in this study is the filtered particle volume fraction. These results are expected to indicate the importance of the TFM closures used in deriving filtered models, as well as contribute to the understanding of how different closures affect the multiphase flow behaviour predicted by resolved TFM simulations of fluidized beds.

2 Simulations

In this section, the methodology used to derive the sub-grid corrections investigated in this study is described. Firstly, the equations used in the resolved simulations are given. Next, the corresponding filtered equations are presented after applying a spatial average to the previous equations. From here, the terms in the filtered equations that require closures, calculated from data from the resolved simulations, are apparent. Additional information about the simulation setup is given, as well as a description of the data analysis procedure necessary to obtain the desired sub-grid corrections as a function of the filtered solids volume fraction.

2.1 Conservation equations

Eulerian two-fluid modelling is used to simulate the flow behaviour inside a periodic section of a fluidised bed, treating the gas and solid phases as separate, continuous phases. The continuity equations for the gas and solid phases are written as follows:

$$\frac{\partial}{\partial t}\left(\alpha_g \rho_g\right) + \nabla \cdot \left(\alpha_g \rho_g \vec{\upsilon}_g\right) = 0 \qquad \text{Equation 1}$$

$$\frac{\partial}{\partial t}\left(\alpha_s \rho_s\right) + \nabla \cdot \left(\alpha_s \rho_s \vec{\upsilon}_s\right) = 0 \qquad \text{Equation 2}$$

Additionally, the sum of the volume fractions for the different phase should be equal to unity. Next, the momentum conservation equation for the gas phase is

$$\frac{\partial}{\partial t}\left(\alpha_g \rho_g \vec{\upsilon}_g\right)+\nabla\cdot\left(\alpha_g \rho_g \vec{\upsilon}_g \vec{\upsilon}_g\right)=-\alpha_g \nabla p+\nabla\cdot\overline{\overline{\tau}}_g+\alpha_g \rho_g \vec{g}+K_{sq}\left(\vec{\upsilon}_s-\vec{\upsilon}_g\right) \qquad \text{Equation 3}$$

And for the solids

$$\frac{\partial}{\partial t}\left(\alpha_s \rho_s \vec{\upsilon}_s\right)+\nabla\cdot\left(\alpha_s \rho_s \vec{\upsilon}_s \vec{\upsilon}_s\right)=-\alpha_s \nabla p-\nabla p_s+\nabla\cdot\overline{\overline{\tau}}_s+\alpha_s \rho_s \vec{g}+K_{gs}\left(\vec{\upsilon}_g-\vec{\upsilon}_s\right) \qquad \text{Equation 4}$$

The inter-phase momentum exchange coefficient $\left(K_{gs}=K_{sg}\right)$ was modelled using three different drag models, namely, the Wen-Yu [18], Huilin-Gidaspow [19] and Syamlal-O'Brien [20] models. The Huilin-Gidaspow model combines the Wen-Yu model with the Ergun equation at solid volume fractions above 0.2. A blending function is used to smooth out the discontinuity between the two equations.

An additional conservation equation is solved for the granular temperature, from which the solids stresses are calculated.

$$\frac{3}{2}\left[\frac{\partial}{\partial t}\left(\alpha_s \rho_s \Theta_s\right)+\nabla\cdot\left(\alpha_s \rho_s \vec{\upsilon}_s \Theta_s\right)\right]=\left(-p_s\overline{\overline{I}}+\overline{\overline{\tau}}_s\right):\nabla\vec{\upsilon}_s+\nabla\cdot\left(k_{\Theta_s}\nabla\Theta_s\right)-\gamma_{\Theta_s}+\phi_{gs} \qquad \text{Equation 5}$$

The first term on the right hand side represents the generation of granular temperature due to normal and shear solids stresses. These stresses are closed by models for the solids pressure [2] and the shear [1] and bulk [2] viscosities. The other terms on the right hand side are the granular conductivity [1] $\left(k_{\Theta_s}\nabla\Theta_s\right)$, the collisional dissipation of kinetic energy [2] (γ_{Θ_s}) and the dissipation of granular temperature due to momentum exchange between the phases [1] (ϕ_{gs}). In the case of dense flows additional solids pressure and viscosity due to prolonged particle contacts can be included by using the frictional pressure model by Johnson & Jackson [21] and the frictional viscosity model by Schaeffer [22]. More accurate frictional models have been proposed in recent years [23], but the Johnson & Jackson formulation was chosen in this study since it is still commonly used in literature due to its simplicity.

The three formulations for the radial distribution that are considered in this study are those by Ogawa [24], Arastoopour [25] and Ma & Ahmadi [26, 27].

To investigate the effect of sub-grid solids structures on the reaction rate, a hypothetical, first-order, solids-catalysed reaction is considered, converting species A into species B. The reaction rate constant is assumed to be independent of temperature and is calculated to produce a meso-scale Thiele modulus (defined as $\varphi=\sqrt{k_{eff}d^2/D}$) of 0.16. The following species conservation equation is solved for the reactant:

$$\frac{\partial}{\partial t}\left(\alpha_g \rho_g X_A\right)+\nabla\cdot\left(\alpha_g \rho_g X_A \vec{\upsilon}_g\right)=\nabla\cdot(D\alpha_g \nabla X_A)-k_A \rho_g \alpha_s X_A \qquad \text{Equation 6}$$

The enthalpy equation is solved to calculate the filtered heat transfer correction. Similar to Agrawal et al. [13], a source term in the solids and an equally-strong sink in the gas phase to conserve energy in the system, was used to maintain a temperature gradient between the phases. The constant Π is selected such that the particles are heated at a rate of $0.1°C/s$. The heat transfer coefficient was calculated from the correlation provided by Gunn [28]. It is assumed that heat conduction due to particle-particle collisions is negligible. Consequently, the following enthalpy equations are solved.

$$\frac{\partial}{\partial t}\left(\alpha_s \rho_s h_s\right)+\nabla\cdot\left(\alpha_s \rho_s h_s \vec{\upsilon}_s\right)=-\gamma(T_s-T_g)+\Pi\alpha_s \qquad \text{Equation 7}$$

$$\frac{\partial}{\partial t}\left(\alpha_g \rho_g h_g\right)+\nabla\cdot\left(\alpha_g \rho_g h_g \vec{\upsilon}_g\right)=\nabla\cdot(k_g\alpha_g\nabla T_g)+\gamma(T_s-T_g)+\Pi\frac{\langle\alpha_s\rangle_d}{\langle\alpha_g\rangle_d}\alpha_g \qquad \text{Equation 8}$$

To keep the calculation of sub-grid scalar fluctuations completely independent from the reactions and heat transfer, an additional scalar variable was solved for each phase. It was assumed that the diffusive flux for the scalars is zero, i.e., scalar quantities are not dispersed by sub-grid-scale fluid or particle motion, or molecular diffusion.

$$\frac{\partial}{\partial t}\left(\alpha_k \rho_k \phi_k\right)+\nabla\cdot\left(\alpha_k \rho_k \vec{\upsilon}_s \phi_k\right)=0 \qquad \text{Equation 9}$$

A similar approach as in ref. [13] was used to impose a mean gradient. In this case, the following substitution was performed: $\phi_k=\phi_k^*+\xi x$, where the value of ξ was chosen as $100m^{-1}$. Substituting this relation into Equation 9, the following conservation equation for the scalar is obtained:

$$\frac{\partial}{\partial t}\left(\alpha_k \rho_k \phi_k^*\right)+\nabla\cdot\left(\alpha_k \rho_k \vec{\upsilon}_s \phi_k^*\right)=-\alpha_k \rho_k \upsilon_{k,x}\phi_k^*\xi \qquad \text{Equation 10}$$

The transport equations are then solved for ϕ_k^*, thus introducing a source term proportional to the phase x-velocity, which is then used to calculate ϕ_k in each cell. The filtered statistics are then calculated for ϕ_k, for which there will always be a mean gradient in the x-direction.

2.2 Filtered conservation equations

The filtered conservation equations are obtained by performing spatial averages on the microscopic conservation equations presented in section 2.1. In the filtered equations, details of the flow structure smaller than the filter size are smoothed out and the effects of the sub-filter scale structures are modelled by closures for new terms appearing in the filtered equations. The filtered equations are then, in principle, capable of predicting the same macroscopic flow behaviour as the resolved simulations, but without having to resolve the small scale multiphase structures using costly, fine grids.

The filtered phase volume fraction is defined as

$$\overline{\alpha_k}(\vec{x},t)=\int_{A_\infty} G(\vec{x},\vec{y})\alpha_k(\vec{y},t)d\vec{y} \qquad \text{Equation 11}$$

where A_∞ is the area of the simulation domain and G, the weight function, is a function of $\vec{x}-\vec{y}$ and is constrained by $\int_{A_\infty} G(\vec{x},\vec{y})d\vec{y}=1$. In this study a simple box filter is used, where G has a constant value within the filter region, extending equally far in the x- and y-directions, and a value of zero outside the filter region. The phase volume is divided into a filtered and a fluctuating part.

$$\alpha_k'(\vec{y},t)=\alpha_k(\vec{y},t)-\overline{\alpha_k}(\vec{y},t) \qquad \text{Equation 12}$$

The following generic equations can also be defined for $\theta'(\vec{y},t)$ and $\tilde{\theta}(\vec{y},t)$, representing any of the conserved variables considered in this study.

$$\overline{\alpha_k}(\vec{x},t)\tilde{\theta}(\vec{x},t) = \int_{A_\infty} G(\vec{x},\vec{y})\alpha_k(\vec{y},t)\theta(\vec{y},t)d\vec{y}$$ Equation 13

$$\theta'(\vec{y},t) = \theta(\vec{y},t) - \tilde{\theta}(\vec{y},t)$$ Equation 14

Based on these definitions, the filtered form of the conservation equations given in section 2.1 can be derived. For the continuity equations, no additional terms are formed that require closure, and the equations are therefore not repeated here. For the solids momentum equation, the filtered equation becomes the following:

$$\frac{\partial}{\partial t}\left(\rho_s\overline{\alpha_s}\widetilde{\vec{\upsilon}_s}\right)+\nabla\cdot\left(\rho_s\overline{\alpha_s}\widetilde{\vec{\upsilon}_s}\widetilde{\vec{\upsilon}_s}\right)=-\overline{\alpha_s}\nabla\overline{p}-\nabla\overline{p_s}-\nabla\cdot\left(\rho_s\overline{\alpha_s\vec{\upsilon}_s'\vec{\upsilon}_s'}\right)$$
$$+\nabla\cdot\overline{\overline{\tau}_s}+\overline{\alpha_s}\rho_s\vec{g}+\overline{K_{gs}\left(\vec{\upsilon}_g-\vec{\upsilon}_s\right)}-\overline{\alpha_s'\nabla p'}$$ Equation 15

Similar filtered stress terms as the third term on the right hand side of the Equation 15 will appear in the gas momentum equation. However, it has been shown that the filtered gas stresses are small compared to the filtered solids stresses [12]. Filtered gas stresses are therefore not compared in this study, in line with ref. [6].

For reasonably large filter sizes, the stresses arising from fluctuations in the particle phase velocities are much larger than the particle stresses arising from the KTGF [29, 30]. Due to the lesser importance of the kinetic theory contributions, the most recent approach has been to also derive closures in terms of filtered markers for the filtered kinetic theory granular pressure and viscosity [31]. In this approach it is no longer necessary to solve the granular temperature equation in the coarse grid fTFM simulations, thereby avoiding having to derive closures for additional terms [8, 15] that would otherwise be required for the filtered granular temperature equation. For this reason, closures for the filtered granular temperature equation are not investigated in this study. It is noted that the important effects of the granular temperature on the cluster/bubble dynamics are already included in the various filtered closures derived from resolved simulations.

The filtered species equation can be written as follows:

$$\frac{\partial}{\partial t}\left(\rho_g\overline{\alpha_g}\widetilde{X_A}\right)+\nabla\cdot\left(\rho_g\overline{\alpha_g}\widetilde{X_A}\widetilde{\vec{\upsilon}_g}\right)=\nabla\cdot(D\overline{\alpha_g\nabla X_A})$$
$$-\nabla\cdot\left(\rho_g\overline{\alpha_g X_A'\vec{\upsilon}_g'}\right)-k_A\rho_g\overline{\alpha_s X_A}$$ Equation 16

The first term on the right can be further divided into a mean and fluctuating part. The fluctuating part would require another closure, but this term is neglected in this study in line with previous studies by the Princeton group. The fluctuation term (second term on the right) is similar in its shape to the fluctuation term arising from the generic scalar transport equation for the gas phase (Equation 18). The filtered energy equation for the solids phase is:

$$\frac{\partial}{\partial t}\left(\rho_s\overline{\alpha_s}\widetilde{h_s}\right)+\nabla\cdot\left(\rho_s\overline{\alpha_s}\widetilde{h_s}\widetilde{\vec{\upsilon}_s}\right)=-\overline{\gamma(T_s-T_g)}+\Pi\overline{\alpha_s}-\nabla\cdot(\rho_s\overline{\alpha_s h_s'\vec{\upsilon}_s'})$$ Equation 17

As can be seen, the source term, i.e., the second term on the right hand side, does not require a closure, while the first term (i.e., that characterizing heat transfer between the phases) does. Similarly to the fluctuation term in the species equation (Equation 16), the third term on the right of Equation 17 can be modelled using the correlation obtained from the generic scalar transport equation presented next:

$$\frac{\partial}{\partial t}\left(\rho_k \overline{\alpha_k}\widetilde{\phi_k}\right)+\nabla\cdot\left(\rho_k \overline{\alpha_k}\widetilde{\phi_k}\widetilde{\vec{\upsilon}_s}\right)=-\nabla\cdot\left(\rho_k \overline{\alpha_k \phi_k{}' \vec{\upsilon}_s{}'}\right)$$ Equation 18

2.3 Filtered closures

2.3.1 Drag and solids stresses

The drag term has been the most important topic of investigation for studies investigating sub-grid corrections for coarse grid simulations. Here we will follow the approach of ref. [12], where the filtered drag force (second last term on the right in Equation 15) and the dynamic part (last term on the right in Equation 15) are lumped together in one sub-grid drag correction factor. Since it would be convenient to implement these two terms in the filtered models as $K_{gs}\left(\widetilde{\vec{\upsilon}_g}-\widetilde{\vec{\upsilon}_s}\right)$, a correlation must be found for the filtered drag correction factor, C, as follows [12]:

$$C=\frac{\overline{K_{gs}\left(\upsilon_{g,y}-\upsilon_{s,y}\right)-\alpha_s{}'\frac{dp'}{dy}}}{K_{gs,coarse}\left(\tilde{\upsilon}_{g,y}-\tilde{\upsilon}_{s,y}\right)}$$ Equation 19

where $K_{gs,coarse}$ is evaluated at the filtered solids volume fraction and filtered slip velocity. Note, that only the forces in the *y*-direction are considered when deriving C, since fluid-particle relative speeds are most significant in this direction.

When considering the solids stresses (third term on the right in Equation 15), the normal components from the x- and y-momentum equations become $\rho_s\overline{\alpha_s\upsilon_{s,x}{}'\upsilon_{s,x}{}'}$ and $\rho_s\overline{\alpha_s\upsilon_{s,y}{}'\upsilon_{s,y}{}'}$ respectively. Assuming isotropic behaviour, a dimensionless filtered solids pressure can be calculated as follows:

$$\hat{p}_{s,fil}=\frac{p_{s,fil}}{\rho_s v_t^2}=\frac{\frac{1}{2}(\overline{\alpha_s\upsilon_{s,x}{}'\upsilon_{s,x}{}'}+\overline{\alpha_s\upsilon_{s,y}{}'\upsilon_{s,y}{}'})}{v_t^2}$$ Equation 20

A closure is still required for the shear stresses arising from the filtered momentum equations. In the work from [6, 9, 13] this term is modelled as a filtered solids viscosity by calculating the ratio of the shear stress and the filtered shear gradients. However, the present study found that this produces a problem in samples in which the filtered shear gradients are small (see section 3.1). Since the present study is only concerned with comparing sub-grid terms for different model formulations, and not with the actual implementation of the filtered models, it was therefore deemed unnecessary to cast the filtered shear stress into the filtered viscosity form. Only the dimensionless filtered solids shear stress is henceforth considered, and calculated as follows:

$$\hat{\tau}_{s,fil}=\frac{\tau_{s,fil}}{\rho_s v_t^2}=\frac{\overline{\alpha_s\upsilon_{s,x}{}'\upsilon_{s,y}{}'}}{v_t^2}$$ Equation 21

It should be noted that closures for the filtered kinetic theory solids pressure and viscosity are also required. However, generally, the contribution from the filtered stresses in Equation 20 and Equation 21 is much larger than the contributions from kinetic theory. Therefore, to limit the scope of this study, closures for the filtered kinetic theory stresses are not considered.

2.3.2 Scalar transport

Previously, a filtered diffusivity has been considered to close the filtered scalar transport equation [13]. In the present study, the same problem with small values for the filtered scalar gradients was experienced as when calculating a filtered solids viscosity (see section 2.3.1). Therefore, only the dimensionless filtered scalar-velocity co-variance (henceforth referred to as the filtered scalar co-variance) is calculated. Note, only the fluctuations of the x-velocity are considered in the present work; an extension to other directions is straight forward and will be considered in future work.

$$\hat{\lambda}_{k,fil} = \frac{\lambda_{k,fil}}{\rho_s v_t} = \frac{\overline{\alpha_k \phi_k' \vec{\upsilon}_s'}}{v_t} \qquad \text{Equation 22}$$

This generic filtered scalar co-variance can be used to model both the filtered dispersion of enthalpy and species in the filtered energy and species equations.

2.3.3 Heat transfer

The filtered heat transfer correction is calculated in a similar way to the filtered drag correction:

$$Q = \frac{\overline{\gamma(T_s - T_g)}}{\gamma_{coarse}\left(\tilde{T}_s - \tilde{T}_g\right)} \qquad \text{Equation 23}$$

where γ_{coarse} is, again, evaluated at the filtered phase volume fraction and filtered slip velocity.

2.3.4 Reactions

A problem that is faced in calculating the filtered reaction rate correction is that X_A tends to zero as the reactant is converted. For this reason, the reactant mass fraction is scaled with the domain averaged reactant mass fraction to produce $\kappa_A = X_A / \langle X_A \rangle_d$. In the present work the approach of ref. [11] is followed, where the filtered reaction rate correction is corrected for non-local effects. Thus, we compute a reaction rate correction as follows:

$$R = \frac{\overline{\alpha_s \kappa_A} - m_2 \nabla \overline{\alpha_s}^T \cdot \nabla \widetilde{\kappa_A}}{\overline{\alpha_s} \widetilde{\kappa_A}} \qquad \text{Equation 24}$$

where $m_2 = \Delta^2 / 12$, and Δ is the filter size. This factor can then be used to correct the last term in Equation 16 for sub-grid effects.

2.4 Solver settings

Simulations are performed using the commercial CFD software, Fluent 16.2.0. Pressure-velocity coupling is performed using the phase-coupled SIMPLE algorithm [32], all other equations are discretised using the QUICK scheme [33]. Second-order implicit time stepping was used since it has previously been shown to be a requirement for time independent solutions of fast, dilute flows [34].

2.5 Simulation geometry

Simulations are performed in a 2D region with dimensions of 0.64 x 0.64 m^2, which was shown to give domain-size independent results by ref. [6]. 2D simulations were performed since the comparison of numerous simulation setups in 3D would be impossible due to the excessive computational requirements of performing simulations in 3D. This approach is justified since it has been found previously that the filtered correlations obtained from 2D simulations are qualitatively similar to those

derived from 3D simulations [6, 9]. 2D simulations will therefore be suitable for the purpose of comparing different resolved TFM setups.

A grid size of 1.25mm x 1.25mm is used, similar to [6, 9]. This corresponds to a length of 16.67 times the particle size, which is insufficient to achieve grid independence according to general guidelines for selecting the grid size in resolved TFM simulations of fluidized beds [4, 35] given the small 75 µm particle size. The computational cost of performing the large number of simulations at different setups required for this study using grid independent simulations remains too high even for 2D simulations. However, performing "slightly unresolved" simulations is valid for this study since it only seeks to compare simulations relative to each other. The error associated with the spatial discretization is hence assumed to be similar in the different simulations.

2.6 Initial and Boundary conditions

The simulation is initiated with a constant solids volume fraction throughout the domain. For each simulation setup investigated, 5 simulations are performed at domain averaged volume fractions of 0.02, 0.1, 0.2, 0.3 and 0.4. A randomly generated particle velocity profile is used during initialization. This speeds up the formation of bubbles/clusters, and therefore allows a shorter simulation time before reaching a pseudo steady state.

The sets of boundaries in the x- and y-directions were selected as periodic. The domain therefore represents a region inside the reactor that is not influenced by wall, inlet or outlet effects. The pressure drop in the vertical direction is controlled to maintain a constant gas superficial velocity, as was previously done for investigating a periodic section of a riser [34].

2.7 Material properties

Material properties similar to those used by the Princeton group were used [6, 9-13]. These properties were assumed to be independent of temperature to eliminate complicated interaction effects and simplify the analysis. The values used are specified in Table 1.

Table 1: The material properties used in this study

d	Particle diameter	75×10^{-6} m
ρ_s	Particle density	1500 kg/m^3
ρ_g	Gas density	1.3 kg/m^3
μ_g	Gas viscosity	1.8×10^{-5} kg/m s
k_g	Gas conductivity	0.024 W/m K
C_{p_g}	Gas heat capacity	1.15×10^{3} J/kg K
C_{p_s}	Particle heat capacity	1×10^{3} J/kg K
D	Mass diffusivity	1.385×10^{-5} m^{-2}/s
v_t	Terminal settling velocity	0.2184 m/s

2.8 Data collection and analysis

The simulations are run for five seconds from an initially slightly perturbed particle velocity distribution until a pseudo steady state is established. After this initial transient period, data regarding important flow properties are written to a file. Specifically, data is probed at the centre of each computational

cell with a probing interval of four characteristic time units, $t_{char} = v_t / g$. Data captured at a specific instant of time is referred to as a 'snapshot'. Due to the very large data output, an efficient method is required to perform the above calculation, and compute filtered (i.e., spatially-averaged) quantities. For this purpose CPPPO (https://github.com/CFDEMproject/C3PO-PUBLIC), a data analysis tool developed by Municchi et al. [36] is used.

When using CPPPO, several filter sizes are specified, and the needed filtering operations are configured. CPPPO can work (i) as a slave during a simulation run, or (ii) can be used as a stand-alone tool to analyse snapshots as done in this work. Filtered values are calculated for multiple filtering operations using each filter size chosen. Filtering operations can be either Favre averages, algebraic averages, or variances. Next, a sampling procedure is defined to calculate the desired quantity, for example the filtered drag correction factor, from the filtered fields. The number of samples collected per sampling operation is the product of the number of cells, the amount of snapshots, and the number of filter sizes specified. Next, the sampled values are binned according to the chosen markers. This is done by dividing the range of marker values in a number of intervals or 'bins'. Each sample is then placed in a bin according to the marker values associated with the sample. Finally, the mean of the values in each bin is calculated.

3 Results and discussions

3.1 Verification against literature results

Since the methodology followed in this paper is strongly based on the papers published by the Princeton group [6, 9-13], the results are compared to ensure that the methodology is applied correctly. Overall, a satisfactory comparison is achieved, indicating that the results generated in the present study can be used with confidence. However, two interesting areas of differences should be addressed.

The first topic involves the modelling of the filtered shear stress for the solids and the filtered co-variance of the scalars. In the work performed at Princeton these quantities were modelled as a filtered solids viscosity and a filtered scalar diffusivity, as follows:

$$\overline{\mu_{s,fil}} = \rho_s \overline{\alpha_s \upsilon_{s,x}' \upsilon_{s,y}'} \Big/ \left(\frac{d\overline{\upsilon_{s,x}}}{dy} + \frac{d\overline{\upsilon_{s,y}}}{dx}\right) \qquad \text{Equation 25}$$

$$\overline{D_{k,fil}} = \rho_s \overline{\alpha_s \phi_k' \upsilon_{k,x}'} \Big/ \left(\frac{d\widetilde{\phi_k}}{dx}\right) \qquad \text{Equation 26}$$

Samples of both of these values become problematic when the value of the denominator is small, resulting in very large sample values. These samples magnify the natural variation in the filtered shear stress and filtered scalar co-variance (numerators in Equation 25 and Equation 26) within each bin and cause problems in obtaining a smooth correlation as a function of the marker. This problem can be reduced by eliminating samples where the denominator has a value below a certain cut-off value. A good comparison with the results from the Princeton group is achieved when using cut-off values equal to the mean gradient ($100m^{-1}$ for this study) for the filtered scalar diffusivity and 1% of the non-dimensional unit for the filtered solids viscosity. However, further investigation of the cut-off values showed that the solution keeps on changing with changing values of the cut-off value.

This is shown in Figure 1 for the filtered scalar diffusivity in the gas phase, although the same is observed for the filtered solids viscosity. It is shown that, initially, increasing the cut-off value leads to a smoother curve. At very large cut-off values, the curves become less smooth again, since a large percentage of the samples are now ignored. It is also clear that the solution keeps changing with the cut-off value. Future research should therefore investigate the closure of the filtered solids shear stresses and filtered scalar co-variances in the form of Equation 25 and Equation 26. However, since this study is only concerned with investigating the effect of different resolved TFM setups relative to each other and not with the implementation of the filtered models, Equation 21 and Equation 22 are considered instead.

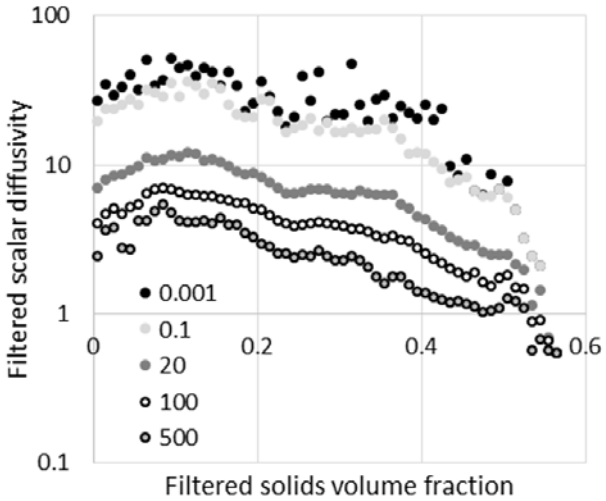

Figure 1 - Comparison of the dimensionless filtered scalar diffusivity in the gas phase considering different values for the cut-off value of the denominator.

Secondly, the main difference in the results from this study and those from Princeton is in the behaviour of the filtered variances at high volume fractions. In the work performed at Princeton, numerous simulations were performed at high domain averaged particle volume fractions. As the domain averaged solids volume fraction is increased above 0.3, a point is reached where the formation of gas bubbles is dramatically reduced and the flow rapidly becomes more homogenous by further increasing the domain averaged volume fraction. In these simulations there are therefore very small variances in each filter region. The correlations derived for the filtered solids pressures, filtered solids viscosity and filtered scalar therefore all peak at a filtered solids volume fraction of approximately 0.3 (with the exception of the scalar diffusivity in the gas phase, which peaks earlier) and then declines towards a zero value at large volume fractions, where the solids distribution is completely homogenous.

These highly homogenous simulations concentrate the samples in a small range of bins around the domain averaged solids volume fraction. In this narrow range of bins, the mean of the sampled values is dragged towards zero, competing with fewer samples obtained from simulations at smaller domain averaged volume fractions. The result is a noticeable dip in the correlation around each domain averaged solids volume fraction considered for large values of the filtered solids volume fraction (this is illustrated to some degree in Figure 2, which will be discussed shortly). To obtain a smooth curve, a large number of domain averaged solids volume fractions would have to be considered as was done

by the Princeton group. However, in the present study where several different model setups are compared, performing that many simulations is not feasible.

For this reason, five domain-averaged solids volume fractions are considered in this study, only up to domain-averaged solids volume fractions where sharp bubbles/clusters still form. This changes the nature of the filtered variances at high filtered solids volume fractions since none of the simulations includes large, dense, slow-moving zones. Instead, very dense regions only occur in small regions inside clusters of particles, where considerable velocity fluctuations still occur. This causes the fluctuations to continue rising above filtered solids volume fraction of 0.3, in contrast to the results of the Princeton group. Regardless of this difference, the values obtained up to filtered solids volume fractions around 0.3 are similar to those reported in ref. [9]. It can therefore be concluded that the nature of the variance terms in dense regions is very different depending on whether the dense region is within a small, dynamic solids cluster or within a large, homogenous solids area, as would occur in dense bubbling beds. Additional markers are clearly necessary to capture this effect and should be investigated in future studies.

At the highest domain average volume fraction of 0.4 considered in this study, clear bubble formation occurs in most model setups. However, when using either the Huilin-Gidaspow or Syamlal-O'Brien drag models, the bubbles in these simulations become much less distinct. This occurs because the interphase momentum exchange coefficient is larger for these models in dense regions than for the Wen-Yu drag model, leading to larger drag forces, smaller slip velocities and more homogenous flow (as discussed in section 3.3.1).

The effect of including the simulation results at a domain averaged solids volume fraction of 0.4 is shown in Figure 2. Results from the simulations with domain averaged volume fractions of 0.3 and 0.4 are shown when analysed individually, as well as the correlation combining data from all domain averaged volume fractions. The results from the two different drag models are quite similar for the data obtained from the domain averaged solids volume fraction of 0.3. On the contrary, it can be seen that, at a domain averaged solids volume fraction of 0.4, the filtered stresses are much smaller in the simulations using the Huilin-Gidaspow drag model due to the more homogenous flow situation with fewer velocity fluctuations. This causes a sharp dip in the correlation around a filtered solids volume fraction of 0.4. Such a sudden change in behaviour makes the comparison of filtered quantities for different model setups difficult. For this reason, the information from simulations using a domain averaged solids volume fraction of 0.4 is neglected in the following results.

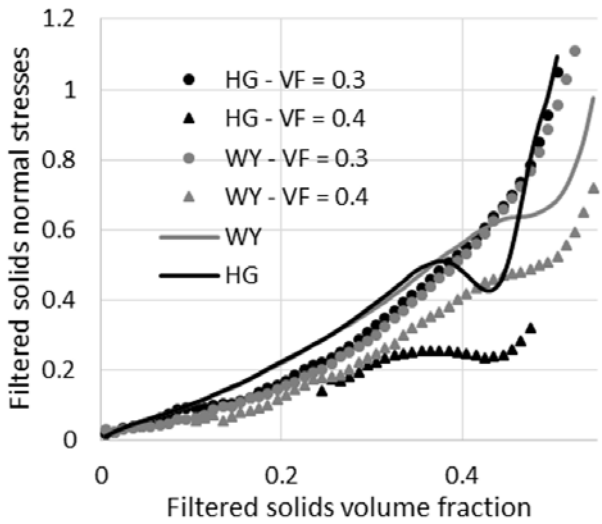

Figure 2 - Comparison of the filtered solids normal stresses for simulations performed with the Wen-Yu and Huilin-Gidaspow drag models using a filter size of 33 by 33 cells.

3.2 Overall impact assessment

This section will give an overall view of the impact of the different TFM setups on the different filtered correlations. This will be done by analysing the difference of the results of each setup from the base case (referred to as Base). The base case was chosen to be similar to the setup employed by the Princeton group in their studies and uses the Wen-Yu drag model, the radial distribution function by Ogawa, a particle-particle restitution coefficient of 0.9 and does not include a frictional pressure model. Additional TFM setups are considered with the following changes from the base case:

- Drag model
  - Huilin-Gidaspow (referred to as the HG case)
  - Syamlal-O'Brien drag model (SO case)
- Frictional pressure
  - Including the frictional pressure model by Johnson & Jackson (FP case)
- Particle-particle restitution coefficient
  - 0.95 (PPR-H)
  - 0.8 (PPR-L)
- Radial distribution functions
  - Arastoopour (Ara)
  - Ma & Ahmadi (MA)

All filtered quantities are presented in their dimensionless forms, as presented in section 2.3. It should also be noted that the filtered slip velocity, $\left|\tilde{\upsilon}_{g,y} - \tilde{\upsilon}_{s,y}\right|$, is also included as one of the filtered quantities to be assessed. The filtered slip velocity has been shown to be an important marker for the drag by ref. [12]. Although not included as a marker in this study, it is expected that it will also be an important marker for other filtered quantities as well, as the filtered slip velocity will influence the shape and definition of the solid clusters and gas bubbles, and thereby also the sub-grid effects. It therefore becomes valuable to assess the influence that different simulations setups will have on the filtered slip velocity.

The overall difference from the base case is quantified by calculating the percentage difference of a filtered quantity from the base case in each bin and then calculating the average difference in all of the bins. However, some bins at large filtered solids volume fractions contain very few samples, causing variation in the data, and should therefore be neglected. To do this, the amount of markers are calculated that would be in each bin if the samples were distributed uniformly over all the bins. All bins with fewer than 20% of this number of samples are then neglected in the comparison of TFM setups and are also not presented in the graphs following in the discussion of results. Such a comparison is given in Figure 3 for a filter size of 9x9 cells (11.25x11.25 mm^2) and in Figure 4 for a filter size of 33x33 cells (41.25x41.25 mm^2).

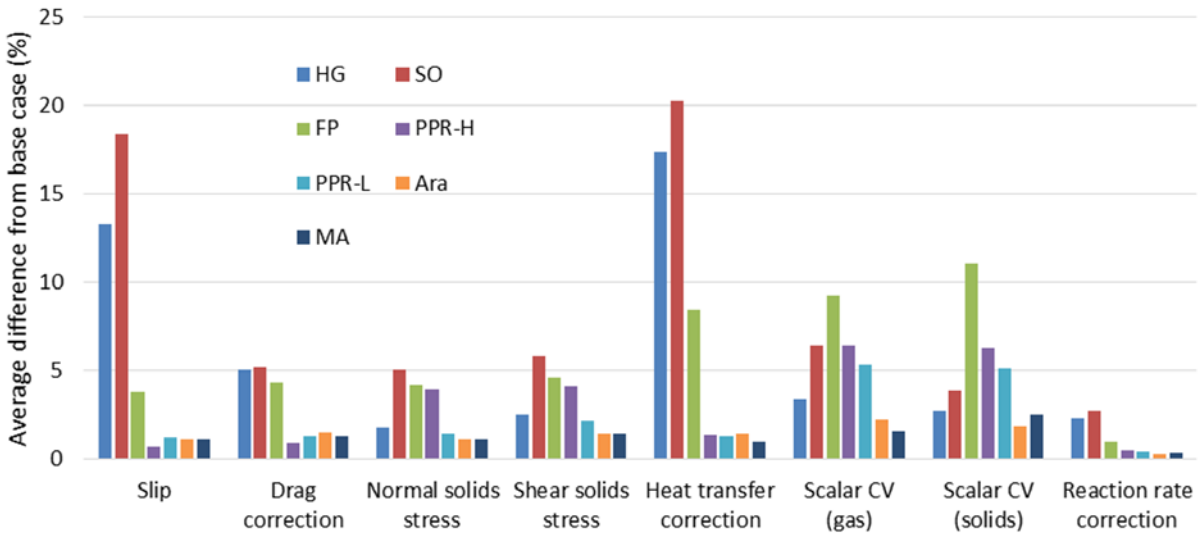

Figure 3 - Comparison of all TFM setups considered to the base case for all filtered quantities using a filter size of 9x9 cells. HG = Huilin-Gidaspow drag model, SO = Syamlal-O'Brien drag model, FP = including frictional pressure, PPR-H = particle-particle restitution coefficient of 0.95, PPR-L = particle-particle restitution coefficient of 0.8, Ara = radial distribution function of Arastoopour, MA = radial distribution function of Ma & Ahmadi.

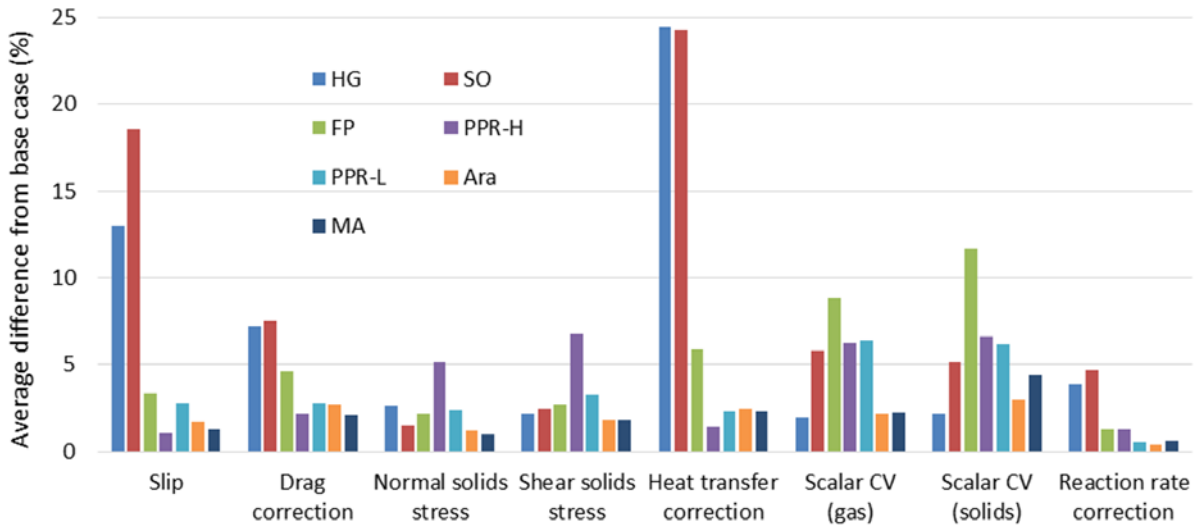

Figure 4 - Comparison of all TFM setups considered to the base case for all filtered quantities using a filter size of 33x33 cells. HG = Huilin-Gidaspow drag model, SO = Syamlal-O'Brien drag model, FP = including frictional pressure, PPR-H = particle-particle restitution coefficient of 0.95, PPR-L = particle-particle restitution coefficient of 0.8, Ara = radial distribution function of Arastoopour, MA = radial distribution function of Ma & Ahmadi.

A number of conclusions can be drawn from this overview of the results generated in this study. Firstly, it is clear that the effect of the drag law (HG and SO) is by far the most important, especially on the filtered slip velocity and filtered heat transfer correction.

Apart from the drag law, however, the average deviations from the base case are relatively small, ranging from about 1% to 10%. The effect of changing the radial distribution function is the smallest and it can in general be concluded that the choice of this closure is insignificant when deriving filtered models. The generally small impact of the TFM formulation on the filtered quantities is a positive result, since it indicates that the uncertainty associated with the choice of the resolved TFM formulation is small in most cases and therefore gives reason for increased confidence in the fTFM approach.

It can also be observed that the effect of the different model settings are mostly similar for the small and the large filter sizes, although there are some exceptions. Firstly, the effect of including frictional pressure (FP) is larger in some cases for the smaller filter size. This is because the frictional pressure is specified to only have an effect at solids volume fractions higher than 0.5. For the large filter size there are fewer samples with very large filtered solids volume fractions, therefore reliable data is available for fewer high filtered solids volume fraction bins. The effect of including the frictional pressure is therefore smaller when using large filter sizes. The significance of changing to the Syamlal-O'Brien drag model is also reduced with the increased filter size. This effect is discussed further in section 3.3.3.

It can also be noted that some filtered quantities are similarly affected by changes in the TFM setup. For example, for the filtered slip velocity, drag correction, heat transfer correction and reaction rate correction, the significant effects are all for the HG, SO and FP cases. Furthermore, the effects on the filtered solid stresses are very similar, with the SO, FP and PPR-H cases being significant. Finally, the two filtered scalar co-variances respond similarly. They also behave somewhat similarly to the filtered solids stresses, except that the frictional pressure (FP) and the lower particle-particle restitution coefficient (PPR-L) has a more significant effect for the filtered scalar co-variances.

These effects will be analysed in more detail in the following section.

3.3 Detailed analysis of significant effects

In this section, the results presented in section 3.2 will be analysed in more detail, limiting the discussion to the more significant model effects on each filtered quantity. The results are visualised by plotting both the filtered quantity and the percentage deviation from the base case as a function of the filtered solids volume fraction. Furthermore, the discussion focusses on the smaller filter size (9x9 cells) since the results are similar for the two filter sizes with some effects more visible for the smaller filter.

3.3.1 Filtered slip velocity

From Figure 5 it can be seen that, at higher filtered solids volume fractions, the filtered slip velocity for the frictional pressure case rapidly decreases relative to the base case. This can be explained through Figure 6 which shows that the dense regions inside clusters tend to be larger and more homogenous when the frictional pressure is included. This is due to the much larger viscosity of the solids in the dense regions with frictional pressure included, causing the solids cluster to become more difficult to deform.

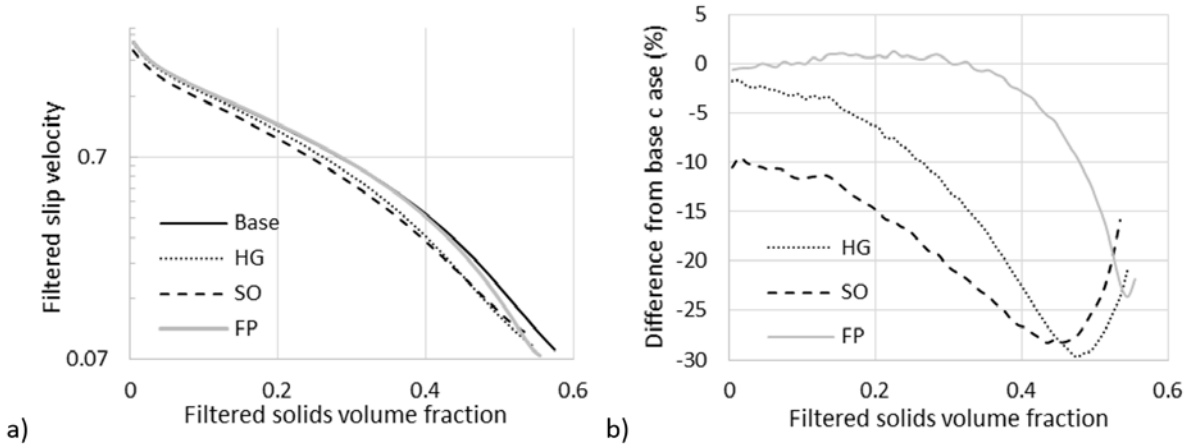

Figure 5 - Comparison of the dimensionless filtered slip velocity for the significant cases by a) the filtered quantity and b) the percentage deviation from the filtered quantity in the base case

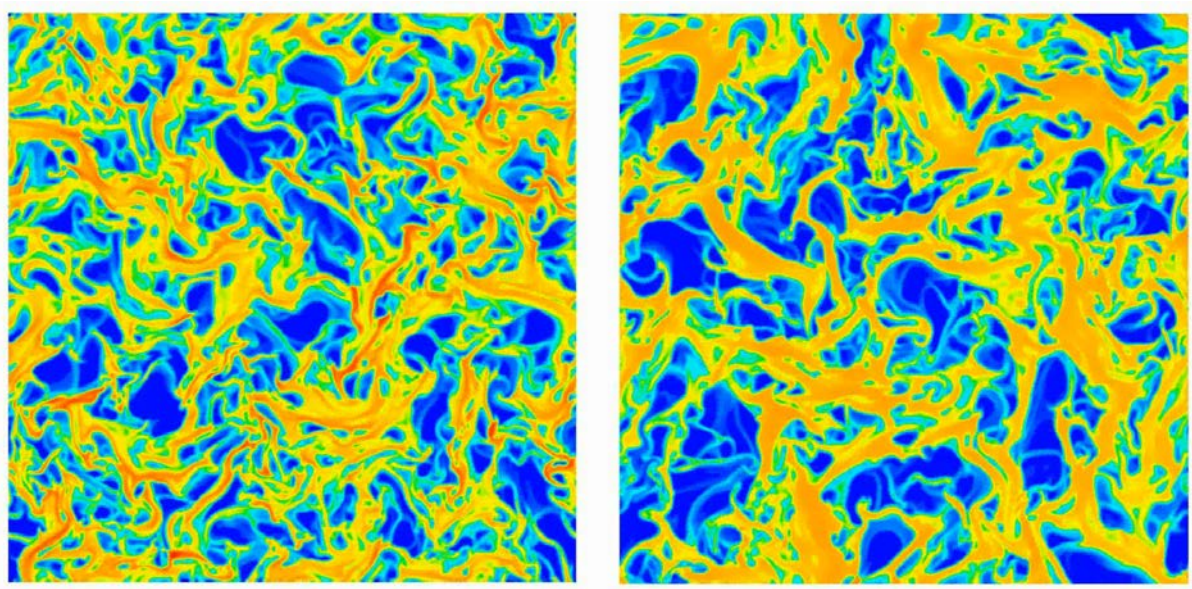

Figure 6 - Comparison of the solids volume fraction contours without frictional pressure on the left and with frictional pressure on the right. Blue corresponds to a solids volume fraction of zero and red to a solids volume fraction of 0.6.

Both the Huilin-Gidaspow and Syamlal-O'Brien drag models predict significantly lower slip velocities over the entire range of filtered volume fractions than the Wen-Yu model, as seen in Figure 5. This behaviour is explained by comparing the interphase momentum exchange coefficients for the drag models, as is done in Figure 7 at a slip velocity of 0.01 m/s (a good approximation of the slip velocities inside the dense regions). Here it can be seen that the interphase exchange coefficient of the Huilin-Gidaspow and Syamlal-O'Brien drag models are larger than that of the Wen-Yu drag model, especially in dense regions. The larger drag forces predicted lead to tighter coupling between the gas and particles, resulting in smaller slip velocities. However, the main reason for the large influence of the alternative drag models is likely to be related to less distinct cluster resolution as will be further discussed in subsequent sections.

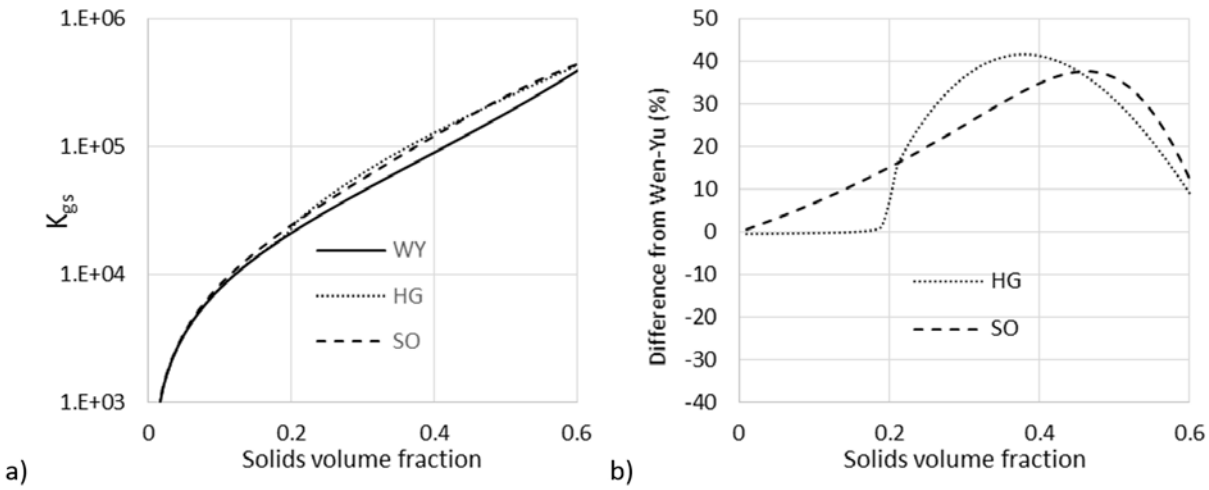

Figure 7 - Comparison of the interphase momentum exchange coefficients for the three drag models considered at a slip velocity of 0.01 m/s by a) the coefficient value and b) the percentage deviation from the Wen-Yu drag law

3.3.2 Filtered drag correction

For the drag correction, the addition of frictional pressure again has a large affect at filtered solids volume fraction above approximately 0.4. This is again due to the more homogenous nature of the cluster with frictional pressure included. In the bins at the highest filtered solids volume fraction with sufficient samples, which corresponds to the centres of the clusters, the solids distribution is essentially uniform and the filtered drag correction is close to unity.

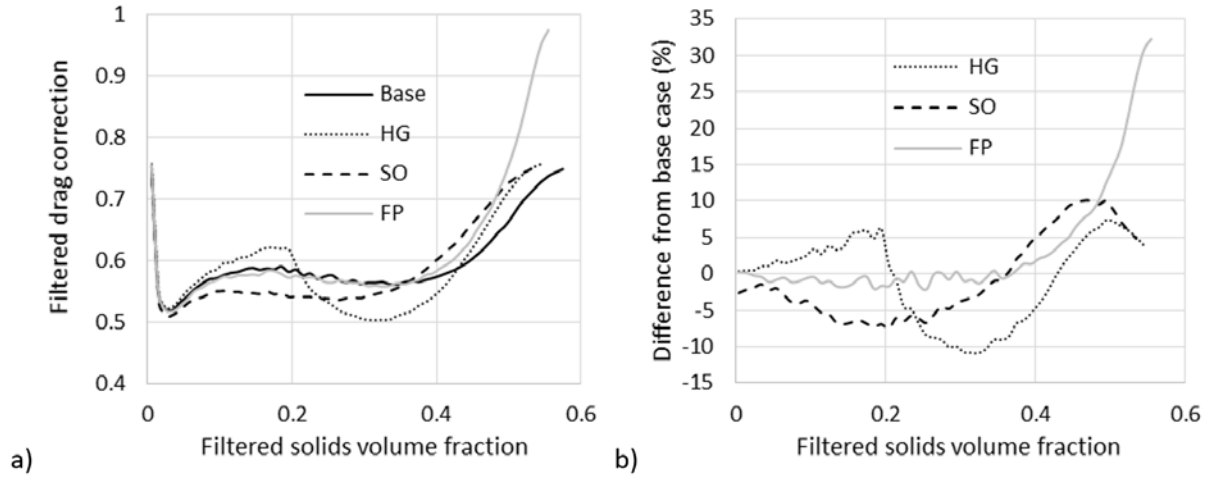

Figure 8 - Comparison of the filtered drag correction for the significant cases by a) the filtered quantity and b) the percentage deviation from the filtered quantity in the base case

The trends for the Huilin-Gidaspow and Syamlal-O'Brien drag models show that the practice of scaling the filtered drag force with the coarse grid drag force appears to work well, since the deviations of the filtered drag corrections fluctuate around zero with a maximum deviation of about 10% in both cases. The shape of the interphase exchange coefficient deviations (right hand side of Figure 7) is clearly visible (inversed) on the right hand side of Figure 8.

It can also be noted that for the cases where frictional pressure is not included, the drag correction factor does not return to a value of 1 near maximum packing. This is due to the nature of the dense regions in this data set where only results from periodic simulations with domain-averaged volume fractions up to 0.3 were included (as previously discussed in section 3.1). Completely homogenous, dense regions that are larger than the filter size therefore do not exist in these simulations (maximum

packing is approached only in small areas inside the clusters). When frictional pressure is included, however, larger clusters form, leading to dense, homogenous regions larger than the filter size and therefore also drag correction factors close to one near maximum packing. The drag correction factor is therefore also expected to return to 1 close to maximum packing for the cases without frictional pressure with the inclusion of more data from denser cases.

3.3.3 Filtered solids stresses

The normal and shear filtered solids stresses behave very similarly, therefore only the shear filtered stress is presented here in Figure 9. Both the normal and shear filtered stresses tend to increase linearly with the filtered solids volume fraction. However, at large values of the filtered solids volume fraction the slope decreases as the velocity fluctuations tend to decrease within the more homogenous regions in the centre of the clusters. This effect is clearly enhanced by including the frictional pressure in the TFM formulation.

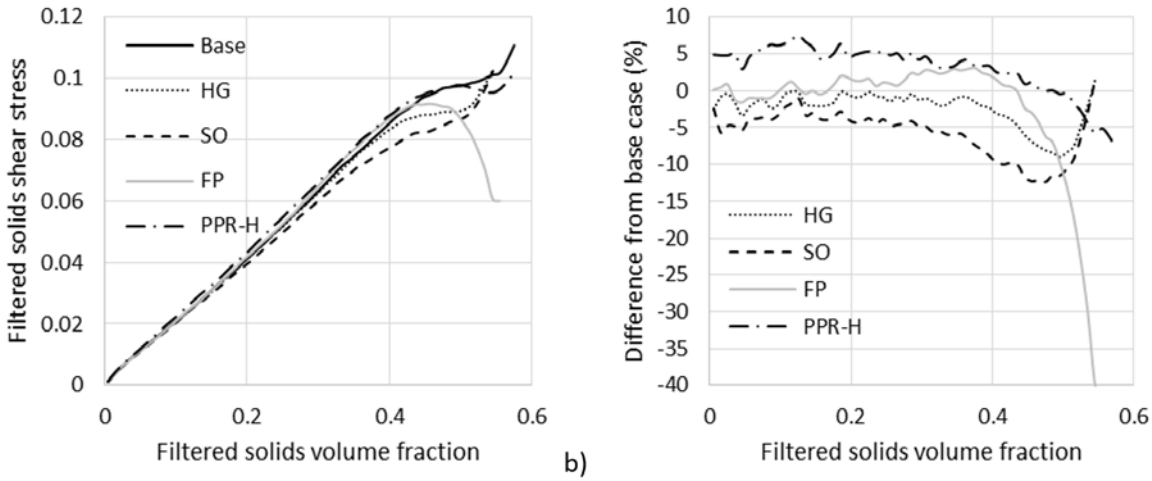

Figure 9 - Comparison of the dimensionless filtered solids shear stress for the significant cases by a) the filtered quantity and b) the percentage deviation from the filtered quantity in the base case

The alternative drag models also tend to decrease the filtered stress in the dense regions. When comparing this result with the filtered slip velocity result in Figure 5, it can be deduced that the influence of the alternative drag laws is to reduce the cluster resolution, especially at higher filtered solids volume fractions. Greater cluster resolution would naturally increase the effects of clustering such as decreased interphase exchange and increased dispersion of mass, momentum and heat. These results clearly show that the use of the Huilin-Gidaspow or Syamlal-O'Brien drag models decrease the filtered slip velocity and the filtered stresses, thus indicating reduced cluster resolution.

Finally, for the filtered stresses the effect of the particle-particle restitution coefficient becomes more significant compared to the other filtered quantities. Discussion of this effect is deferred to section 3.3.5 where both the low and high particle-particle restitution coefficient cases were significant.

3.3.4 Filtered heat transfer correction

Similar to the filtered drag correction, the inclusion of frictional pressure causes the filtered heat transfer correction to proceed to unity at large filtered solids volume fractions (Figure 10). However, for the case of the filtered heat transfer correction, there is a region around filtered solids volume fractions of 0.3 where the correction is actually predicted to be larger. This may be due to the much more viscous solids phase in the dense particle regions which restrict convective heat transfer.

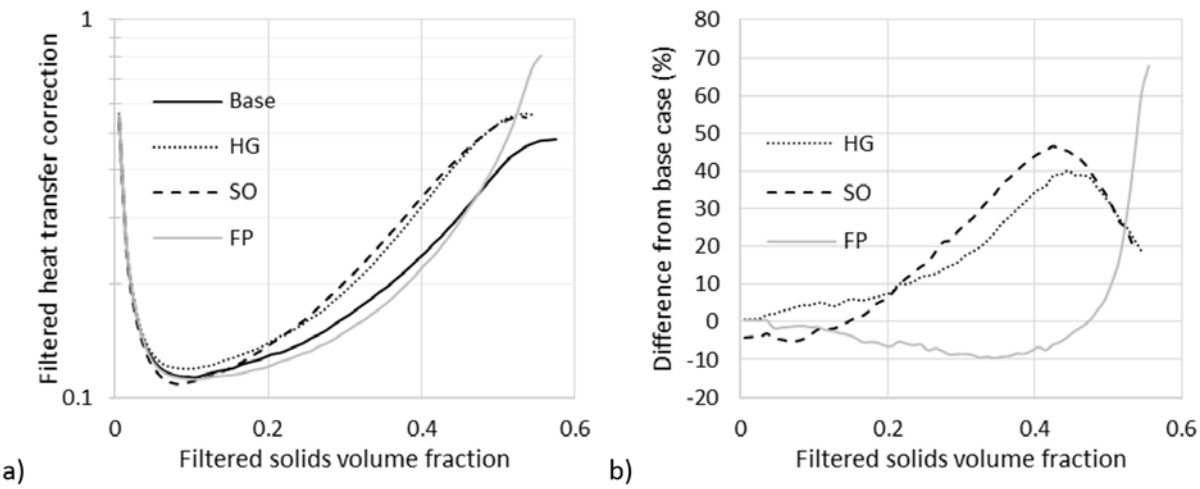

Figure 10 - Comparison of the filtered heat transfer correction for the significant cases by a) the filtered quantity and b) the percentage deviation from the filtered quantity in the base case

For the drag laws, both the Huilin-Gidaspow and Syamlal-O'Brien predict substantially smaller sub-grid drag corrections than the Wen-Yu drag model. This is again due to the degree of cluster resolution being lower with these drag models as discussed in the previous section.

3.3.5 Filtered scalar co-variances

Figure 11 and Figure 12 show the filtered scalar co-variances in the gas and solid phases, respectively. It can be noted that filtered scalar co-variance in the solids phase behave similarly to the solids shear stress, except for an increase of the slope at very large filtered solids volume fractions. The shape of the filtered correlation is very different in the gas phase. However, despite this difference, the effect of changes in the resolved TFM formulation is very similar. The effects of the frictional pressure and the two alternative drag laws can therefore be explained through similar arguments to those put forward in section 3.3.3.

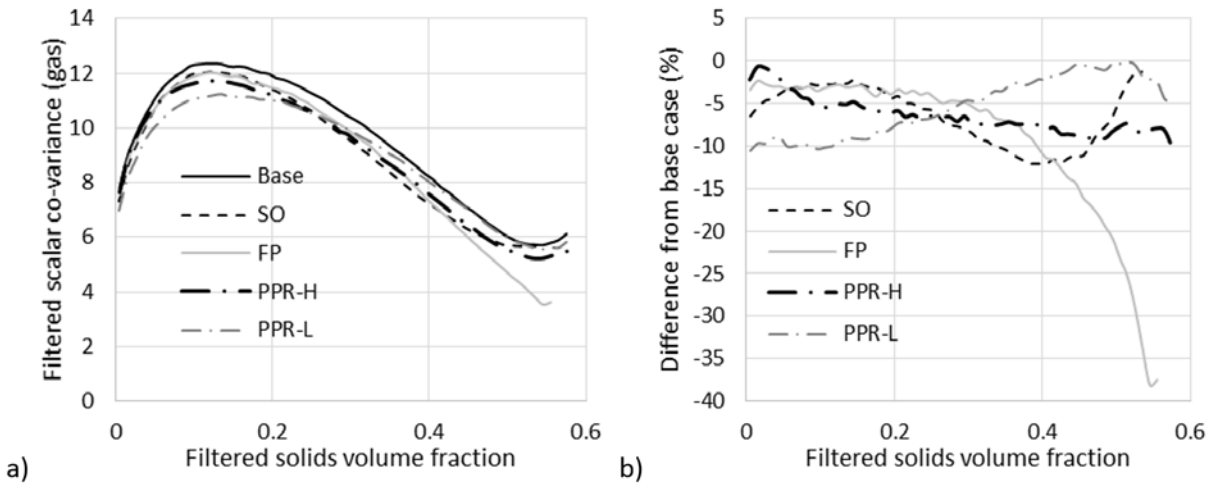

Figure 11 - Comparison of the filtered scalar co-variance in the gas phase for the significant cases by a) the filtered quantity and b) the percentage deviation from the filtered quantity in the base case

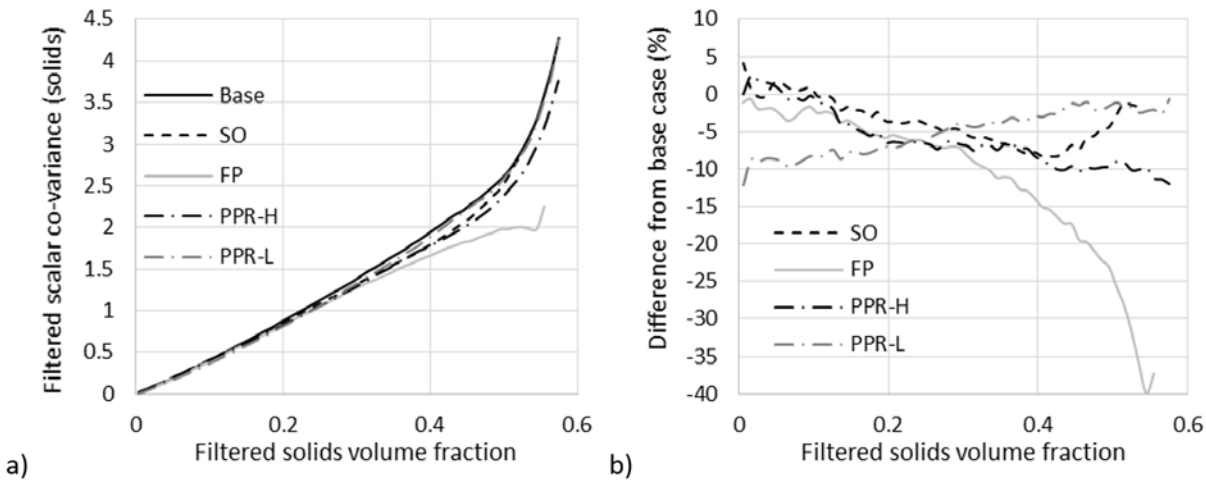

Figure 12 - Comparison of the filtered scalar co-variance in the particle phase for the significant cases by a) the filtered quantity and b) the percentage deviation from the filtered quantity in the base case

The effect of changing the particle-particle restitution coefficient, however, requires additional discussion. Unlike the filtered solids stresses, more elastic collisions now lead to smaller filtered scalar co-variances. A similar decrease is observed when the particle-particle restitution coefficient is decreased to 0.8 from 0.9. However, the particle-particle restitution coefficient of 0.95 leads to a maximum decrease in the filtered scalar co-variance at high filtered solids volume fractions, while a particle-particle restitution coefficient of 0.8 leads to a maximum decrease in the dilute regions.

To gain a better understanding of this behaviour, the solids volume fraction variance ($\overline{\alpha_s' \alpha_s'}$) was calculated for the three cases with different particle-particle restitution coefficients. For the case with the less elastic collisions, both the non-homogeneity of the solids and the scalar dispersion tends to increase relative to the base case from low solids volume fractions to high solids volume fraction, since the less elastic collisions lead to more clustering in the dense regions. Surprisingly, however, the scalar dispersion is decreased relative to the base case, whereas one would expect the increased variance in the solids volume fraction to lead to more scalar dispersion.

In the case of the more elastic collisions, the solids volume fraction variance is decreased relative to the base case in the dilute regions due to decreased clustering. The scalar variance decreases relative to the base case, but in contrast to the solids volume fraction variance, this decrease takes place in the dense regions. It can therefore be concluded that the scalar dispersion is not influenced only by the degree of volume fraction segregation and that other factors, such as the cluster shape, size and number, play an important role. Further investigations using additional markers will be required to fully understand these trends.

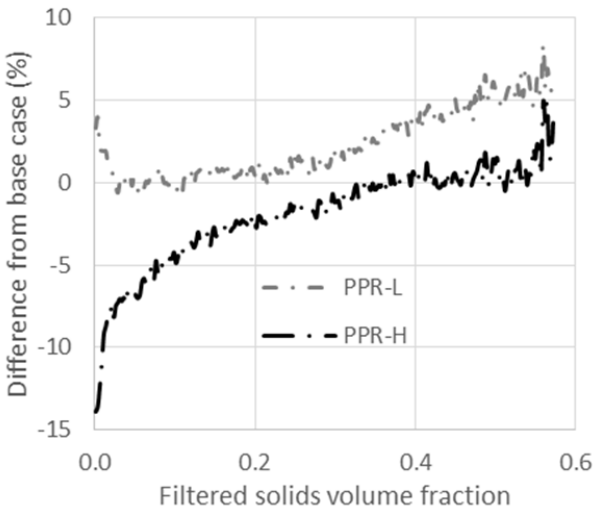

Figure 13 - Percentage deviation of the solids volume fraction variance from that in the base case

3.3.6 Filtered reaction correction

The effect of changes in the TFM formulation is nearly identical for the filtered heat transfer and filtered reaction rate correction (Figure 14). This is understandable, since interphase heat transfer and first-order, solids catalysed reaction are analogous processes. However, the changes caused by the different TFM formulations are much smaller for the filtered reaction rate correction. This is because the reaction rate chosen is relatively slow compared to the heat transfer rate.

Figure 14 - Comparison of the filtered reaction rate correction in the gas phase for the significant cases by a) the filtered quantity and b) the percentage deviation from the filtered quantity in the base case

4 Summary and conclusions

In this study, the effect that different resolved TFM formulations have on the filtered correlations derived from them were evaluated. Different model selections were tested for the drag law, frictional pressure, particle-particle restitution coefficient and radial distribution function. The effects of changing these model formulations were then evaluated by considering the average difference in several filtered quantities compared to a base case. The filtered quantities considered included the slip velocity; drag, heat transfer and reaction rate corrections, normal and shear solids stresses and scalar co-variances in the gas and solids phases.

The primary conclusion from this study is that generally the average change in filtered correlations with different resolved TFM formulations is small, 1 to 12% for all factors excluding the drag. This provides reason for increased confidence in the fTFM approach, since it indicates that fTFMs are not very susceptible to uncertainties in the choice of TFM closures used in the resolved simulations from which the filtered models are derived.

A larger effect was observed for the drag model: approximately 20% average deviation from the base case. This is an important finding since there is not yet consensus in the literature regarding the best choice of drag model and therefore several different drag models are commonly used. Inclusion of a frictional pressure model also had a significant effect, with average differences from the base case in the range of 4% to 12%. However, these difference are mostly present in the very large solids volume fraction range where differences can increase up to 70% due to larger, more viscous solids clusters

when frictional pressure is included. Inclusion of a frictional pressure model is therefore also recommended for future studies.

Finally, it was noted that the filtered quantities could be divided into two groups according to how they reacted to changes in the resolved TFM formulations. The filtered drag, heat transfer and reaction corrections were significantly influenced by the choice of drag law and the inclusion of frictional pressure. The quantities containing variances, the filtered solids stresses and filtered scalar co-variances, were significantly affected by changes in the drag law, inclusion of frictional pressure and changes in the particle-particle restitution coefficient. The similar behaviour within groups suggests that the transport processes within each group are controlled by the same mechanisms. This knowledge may be used when selecting markers and formulating closures for filtered quantities within these groups.

5 Acknowledgements

The authors would like to express their gratitude for the financial support from the European Commission under the NanoSim grant (project number: 604656), as well as for the computational resources provided at NTNU by UNINETT Sigma2 AS, https://www.sigma2.no.

6 List of Acronyms and Symbols

Acronym definitions:

CFD	Computational Fluid Dynamics
CV	Co-variance
fTFM	Filtered Two-fluid Model
KTGF	Kinetic Theory of Granular Flow
TFM	Two-fluid Model
UDS	User-defined scalar

Main Symbol definitions:

C	Filtered drag correction factor
C_p	Heat capacity (J/kg K)
D	Mass diffusivity (m^2/s)
d	Particle diameter (m)
G	Weight function
$\vec{g}$	Gravity vector (m/s^2)
g_0	Radial distribution function

h	Specific enthalpy (J/kg)
K_{sg}	Interphase momentum exchange coefficient (kg/m^{3}s)
k_A	Reaction rate constant of species A
k_g	Gas phase thermal conductivity (W/m K)
k_{Θ_s}	Granular temperature diffusion coefficient (kg/m s)
p	Pressure (Pa)
Q	Filtered heat transfer correction factor
R	Filtered reaction rate correction factor
t	Time (s)
v_t	Particle terminal velocity (m/s)
X_A	Mass fraction of species A
x	Distance in the x-direction (m)
$\vec{x}, \vec{y}$	Position vector
α	Volume fraction
ϕ	Generic scalar
ϕ_{gs}	Interphase energy transfer (W/m^3)
φ	Thiele modulus
γ	Heat transfer coefficient (W/m^3)
γ_{Θ_s}	Dissipation rate (W/m^3)
κ_A	Mass fraction of A scaled with domain averaged mass fraction
λ	Filtered scalar-velocity co-variance (m/s)
μ	Dynamic viscosity (kg/m s)
ρ	Density (kg/m^2)
τ	Filtered shear stress (m^2/s^2)
$\bar{\bar{\tau}}$	Stress tensor (Pa)

$\vec{\upsilon}$ Velocity vector (m/s)

ξ Gradient constant (m^{-1})

Δ Filter size (m)

Π Heat transfer source term constant (W/m^3)

Θ Granular temperature (m^2/s^2)

Sub- and superscript definitions:

fil Filtered variable

g Gas

k Generic phase

s Solid

Operator definitions

$\bar{x}$ Volume average

$\tilde{x}$ Favre average

x' Fluctuation from mean

$\langle x \rangle_d$ Domain average

$\hat{x}$ Non-dimensionalised value

$\vec{x}$ Vector quantity

7 References

[1] D. Gidaspow, R. Bezburuah, J. Ding, Hydrodynamics of Circulating Fluidized Beds, Kinetic Theory Approach, 7th Engineering Foundation Conference on Fluidization 1992, pp. 75-82.

[2] C.K.K. Lun, S.B. Savage, D.J. Jeffrey, N. Chepurniy, Kinetic Theories for Granular Flow: Inelastic Particles in Couette Flow and Slightly Inelastic Particles in a General Flow Field, J. Fluid Mech., 140 (1984) 223-256.

[3] J.L. Sinclair, R. Jackson, Gas-particle flow in a vertical pipe with particle-particle interactions, AIChE J., 35 (1989) 1473-1486.

[4] S. Cloete, S.T. Johansen, S. Amini, Grid independence behaviour of fluidized bed reactor simulations using the Two Fluid Model: Effect of particle size, Powder Technol., 269 (2015) 153-165.

[5] N. Yang, W. Wang, W. Ge, L. Wang, J. Li, Simulation of Heterogeneous Structure in a Circulating Fluidized-Bed Riser by Combining the Two-Fluid Model with the EMMS Approach, Ind. Eng. Chem. Res., 43 (2004) 5548-5561.

[6] Y. Igci, A.T. Andrews, S. Sundaresan, S. Pannala, T. O'Brien, Filtered two-fluid models for fluidized gas-particle suspensions, AIChE J., 54 (2008) 1431-1448.

[7] J.-F. Parmentier, O. Simonin, O. Delsart, A functional subgrid drift velocity model for filtered drag prediction in dense fluidized bed, AIChE J., 58 (2012) 1084-1098.
[8] A. Ozel, P. Fede, O. Simonin, Development of filtered Euler–Euler two-phase model for circulating fluidised bed: High resolution simulation, formulation and a priori analyses, Int. J. Multiphase Flow, 55 (2013) 43-63.
[9] Y. Igci, S. Sundaresan, Constitutive Models for Filtered Two-Fluid Models of Fluidized Gas–Particle Flows, Ind. Eng. Chem. Res., 50 (2011) 13190-13201.
[10] Y. Igci, S. Sundaresan, Verification of filtered two-fluid models for gas-particle flows in risers, AIChE J., 57 (2011) 2691-2707.
[11] W. Holloway, S. Sundaresan, Filtered models for reacting gas–particle flows, Chem. Eng. Sci., 82 (2012) 132-143.
[12] C.C. Milioli, F.E. Milioli, W. Holloway, K. Agrawal, S. Sundaresan, Filtered two-fluid models of fluidized gas-particle flows: New constitutive relations, AIChE J., 59 (2013) 3265-3275.
[13] K. Agrawal, W. Holloway, C.C. Milioli, F.E. Milioli, S. Sundaresan, Filtered models for scalar transport in gas–particle flows, Chem. Eng. Sci., 95 (2013) 291-300.
[14] S. Schneiderbauer, S. Puttinger, S. Pirker, Comparative analysis of subgrid drag modifications for dense gas-particle flows in bubbling fluidized beds, AIChE J., 59 (2013) 4077-4099.
[15] S. Schneiderbauer, S. Pirker, Filtered and heterogeneity-based subgrid modifications for gas–solid drag and solid stresses in bubbling fluidized beds, AIChE J., 60 (2014) 839-854.
[16] S. Cloete, S. Amini, S.T. Johansen, A fine resolution parametric study on the numerical simulation of gas-solid flows in a periodic riser section, Powder Technol., 205 (2011) 103-111.
[17] S. Schneiderbauer, S. Pirker, The impact of different fine grid simulations on the sub-grid modification for gas–solid drag, 9th International Conference on Multiphase FlowFirenze, 2016.
[18] C.Y. Wen, Y.H. Yu, Mechanics of Fluidization, Chem. Eng. Prog. S. Ser., 62 (1966) 100-111.
[19] L. Huilin, D. Gidaspow, Hydrodynamics of binary fluidization in a riser: CFD simulation using two granular temperatures, Chem. Eng. Sci., 58 (2003) 3777-3792.
[20] M. Syamlal, T.J. O'Brien, Computer simulation of bubbles in a fluidized bed, AIChE Symposium Series, 1989, pp. 22-31.
[21] P.C. Johnson, R. Jackson, Frictional-Collisional Constitutive Relations for Granular Materials, with Application to Plane Shearing, J. Fluid Mech., 176 (1987) 67-93.
[22] D.G. Schaeffer, Instability in the Evolution Equations Describing Incompressible Granular Flow, J. Differ. Equations, 66 (1987) 19-50.
[23] S. Schneiderbauer, A. Aigner, S. Pirker, A comprehensive frictional-kinetic model for gas–particle flows: Analysis of fluidized and moving bed regimes, Chem. Eng. Sci., 80 (2012) 279-292.
[24] S. Ogawa, A. Unemura, N. Oshima, On the Equation of Fully Fluidized Granular Materials, J. Appl. Math. Phys, 31 (1980) 483.
[25] H. Iddir, H. Arastoopour, Modeling of multitype particle flow using the kinetic theory approach, AIChE J., 51 (2005) 1620-1632.
[26] G. Ahmadi, D. Ma, A thermodynamical formulation for dispersed multiphase turbulent flows—1, Int. J. Multiphase Flow, 16 (1990) 323-340.
[27] D. Ma, G. Ahmadi, A thermodynamical formulation for dispersed multiphase turbulent flows—II, Int. J. Multiphase Flow, 16 (1990) 341-351.
[28] D.J. Gunn, Transfer of Heat or Mass to Particles in Fixed and Fluidized Beds, International Journal of Heat and Mass Transfer, 21 (1978) 467-476.
[29] K. Agrawal, P.N. Loezos, M. Syamlal, S. Sundaresan, The Role of Meso-Scale Structures in Rapid Gas-Solid Flows, J. Fluid Mech., 445 (2001) 151-185.
[30] A.T. Andrews, P.N. Loezos, S. Sundaresan, Coarse-grid simulation of gas-particle flows in vertical risers, Industrial and Engineering Chemistry Research, 44 (2005) 6022-6037.
[31] A. Sarkar, F.E. Milioli, S. Ozarkar, T. Li, X. Sun, S. Sundaresan, Filtered sub-grid constitutive models for fluidized gas-particle flows constructed from 3-D simulations, Chem. Eng. Sci., 152 (2016) 443-456.
[32] S. Patankar, Numerical Heat Transfer and Fluid Flow, Hemisphere Publishing Corporation1980.

[33] B.P. Leonard, S. Mokhtari, ULTRA-SHARP Nonoscillatory Convection Schemes for High-Speed Steady Multidimensional Flow, NASA TM 1-2568 (ICOMP-90-12)NASA Lewis Research Center, 1990.
[34] S. Cloete, S. Amini, S.T. Johansen, On the effect of cluster resolution in riser flows on momentum and reaction kinetic interaction, Powder Technol., 210 (2011) 6-17.
[35] S. Cloete, S.T. Johansen, S. Amini, Grid independence behaviour of fluidized bed reactor simulations using the Two Fluid Model: Detailed parametric study, Powder Technol., 289 (2016) 65-70.
[36] F. Municchi, C. Goniva, S. Radl, Highly efficient spatial data filtering in parallel using the opensource library CPPPO, Computer Physics Communications, 207 (2016) 400-414.